Bioorganic & Medicinal Chemistry 23 (2015) 7464–7477

Contents lists available at ScienceDirect

Bioorganic & Medicinal Chemistry

journal homepage: www.elsevier.com/locate/bmc

Discovery of bis-aryl urea derivatives as potent and selective Limk inhibitors: Exploring Limk1 activity and Limk1/ROCK2 selectivity through a combined computational study

Jiaxin Cui [a], Mei Ding [a], Wei Deng [a], Yan Yin [a,b,*], Zhonghua Wang [a], Hong Zhou [a], Guofeng Sun [a], Yu Jiang [a], Yangbo Feng [c]

[a] School of Chemical and Environmental Engineering, Shanghai Institute of Technology, 100 Hai Quan Rd, Shanghai 201418, PR China
[b] Key Laboratory of Synthetic Chemistry of Natural Substances, Shanghai Institute of Organic Chemistry, Chinese Academy of Sciences, 345 Ling Ling Rd, Shanghai 200032, PR China
[c] Medicinal Chemistry, Translational Research Institute, The Scripps Research Institute, Florida, Jupiter, FL 33458, USA

ARTICLE INFO

Article history:
Received 30 September 2015
Revised 28 October 2015
Accepted 29 October 2015
Available online 30 October 2015

Keywords:
Limk1 inhibitors
Limk1/ROCK2 selectivity
Urea derivatives
Molecular modeling
Molecular docking

ABSTRACT

Lim kinase (Limk), a proline/serine-rich sequence, can regulate the polymerization of the actin filaments by phosphorylating, and it is found to be highly involved in various human diseases. In this paper, 47 reported Limk1 inhibitors with bis-aryl urea scaffold were used to design potent and selective Limk inhibitors by computational approaches. Firstly, the structure-Limk1 activity relationship models (3D-QSAR) and structure-Limk1/ROCK2 selectivity relationship models (3D-QSSR) were developed and both 3D-QSAR and 3D-QSSR models showed good correlative and predictive abilities. Then, the molecular docking and molecular dynamics (MD) simulations were employed to validate the optimal docking conformation and explore the binding affinities. Finally, five new compounds were designed and all of them exhibited good Limk1 inhibition and Limk1/ROCK2 selectivity after synthesis and biological evaluation, which demonstrated that the obtained information from computational studies were valuable to guide Limk inhibitors' design.

© 2015 Elsevier Ltd. All rights reserved.

1. Introduction

LIM Kinase (Limk) is a serine-threonine protein and two isoforms are identified as Limk1 and Limk2.[1,2] The structure of Limk have been solved by solution NMR or X-ray diffraction,[3] which consists of two amino-terminal LIM domains, adjacent PDZ and proline/serine-rich regions, following by a carboxyl-terminal protein kinase domain. Limk is downstream of ROCK and PAK,[4] and regulate the polymerization of actin filaments in the signaling pathways.[5–9] Activated Limk can phosphorylate and inactivate cofilin, thereby lead a dynamic regulation of actin cytoskeleton. Accumulated evidence suggests that many disorders are correlated to the regulator mechanism of Limk and the Limk inhibitors will be potential drugs for a variety of human diseases including syndrome,[10] Alzheimer's disease,[11] Parkinson's disease,[12] Williams' disease,[13] psoriatic epidermal lesions,[14] preeclampsia' disease,[15] intracranial aneurysms,[16] ocular hypertension/glaucoma,[17] HIV and other viral infections,[18–20] and tumors.[21–27]

Although lots of studies about Limk were been done in recent years,[2,17,28–39] to the best of our knowledge few Limk inhibitors were described.[2,17,28–36] Very recently our group reported aryl urea derivatives as potent and selective Limk inhibitors.[40] We also disclosed aryl ureas as ROCK inhibitors and explored their ROCK2/PKA selectivity by 3D-QSAR, molecular docking and molecular dynamic simulation.[41] In this work, we will reveal the structural and chemical properties that favor Limk1 inhibition and the Limk1/ROCK2 selectivity for aryl urea derivatives through several computational approaches. Comparative molecular field analyses (CoMFA) and comparative molecular similarity indices analyses (CoMSIA) are applied to obtain insights into key structural factors that affect the inhibitory activity and selectivity of aryl urea based Limk inhibitors. Molecular docking followed by molecular dynamics (MD) simulations are then conducted to validate the models and to further explore the origin of the selectivity at the amino acid residue level. Finally, the residues which introduced ligand potency and Limk1/ROCK2 selectivity are discovered and further validated by chemical synthesis and biological evaluation. Herein, the computer-aided drug design of highly potent and selective Limk inhibitors will be described in detail, and the synthetic procedures and structural characterization of the newly designed com-

* Corresponding author. Tel.: +86 21 60877220; fax: +86 21 60877231.
E-mail address: yinyan@sit.edu.cn (Y. Yin).

http://dx.doi.org/10.1016/j.bmc.2015.10.041
0968-0896/© 2015 Elsevier Ltd. All rights reserved.

pounds will also be reported along with the biological experimental protocols.

2. Results and discussion

2.1. Data set

Chemical structures and IC_{50} values against Limk1 and ROCK2 of 47 reported Limk inhibitors were listed in Table 1.[40] Forty compounds with accurate Limk1 inhibitory activity were chosen to build quantitative structure-Limk1 activity relationship (3D-QSAR) models and sorted into training set and test set randomly (30 compounds into training set and 10 compounds into test set). Twenty two compounds with accurate Limk1 and ROCK2 inhibition IC_{50} values were collected for quantitative structure-Limk1/ROCK2 selectivity relationship (3D-QSSR) models and also sorted randomly (17 into training set and 5 into test set).[42]

2.2. Statistical results

Since compound **47** was the most active Limk1 inhibitor and **36** was one of the most Limk1/ROCK2 selective Limk1 inhibitors among those in Table 1, they were used as the reference compounds for 3D-QSAR models and 3D-QSSR models, respectively. Models including CoMFA 3D-QSAR models, CoMSIA 3D-QSAR models, CoMFA 3D-QSSR models, and CoMSIA 3D-QSSR models were developed and optimal models were chosen according to the statistical parameter after the partial least square (PLS) analysis. The q^2 (cross-validated correlation coefficient), r^2 (correlation coefficient), see (standard error of estimate), and *F*-value ($r^2/1 - r^2$) were 0.618, 0.995, 0.06, and 501.848 for the chosen CoMFA 3D-QSAR model, 0.572, 0.943, 0.185, and 80.136 for the chosen CoMSIA 3D-QSAR model, 0.561, 0.995, 0.058, and 273.753 for the chosen CoMFA 3D-QSSR model, and 0.541, 0.994, 0.068, and 199.531 for the chosen CoMSIA 3D-QSSR model, respectively, (Table 2). The q^2 values of all the chosen models were more than 0.5 which indicated that these chosen models were reliable and predictive.

The contribution was 0.441 for steric field and 0.559 for electrostatic field in CoMFA 3D-QSAR model, and the contribution was 0.407 for steric field and 0.593 for electrostatic field in CoMFA 3D-QSSR model, so electrostatic field was the main contribution in CoMFA models. The contributions of steric field, electrostatic field, H-acceptor, H-donor, and hydrophobic field were 0.116, 0.369, 0.139, 0.186, 0.191 in CoMSIA 3D-QSAR model, and 0.137, 0.167, 0.139, 0.104, and 0.453 in CoMSIA 3D-QSSR model, respectively, (Table 2).

Limk1 inhibition activity ($pIC_{50Limk1}$), residual of Limk1 inhibition activity ($\Delta pIC_{50activity}$), and residual rate of Limk1 inhibition activity were calculated and listed in 3D-QSAR models of Table 3. Limk1/ROCK2 selectivity ($\Delta pIC_{50selectivity}$), residual of Limk1/ROCK2 selectivity ($\Delta\Delta pIC_{50selectivity}$), and residual rate of Limk1/ROCK2 selectivity were calculated and listed in 3D-QSSR models of Table 3. In 3D-QSAR models, residuals were between −0.403 and 0.304 and residual rates were between −6.1% and 4.1% for the training set, and residuals were between −0.657 and 0.831 and residual rates were between −9.9% and 12% for the test set. In 3D-QSSR models, residuals were between −0.061 and 0.132 and the residual rates were between −5% and 10.6% for the training set, and residuals were between −0.519 and 0.433 and the residual rates were between −29% and 35% for the test set. Although the range of residual rates in the test set of 3D-QSSR model were a little bit broader than others (−29% to 35% vs −6.1% to 4.1%, −5% to 10.6% and −9.9% to 12%), all models including 3D-QSAR model and 3D-QSSR model exhibited good correlative and predictive power.

The correlations between the experimental and predicted values of CoMFA 3D-QSAR model, CoMSIA 3D-QSAR model, CoMFA 3D-QSSR model and CoMSIA 3D-QSSR model were exhibited in Figure 1. Most points were well distributed along the line $Y = X$ also suggested that all chosen models for this work were correlative and predictive.

2.3. Counter maps analysis

For the convenience of counter maps analysis, the urea-based Limk1 inhibitors were divided into five regions: R_1 region, R_2 region, R_3 region, R_4 region, and Ar region, and the structure–activity/selectivity relationships derived from 3D-QSAR and 3D-QSSR studies were summarized in Figure 2.

2.3.1. Contour maps of steric field

The steric field contour maps were shown in Figure 3. As shown in Figure 3A and B, there was a big green contour around the N atom (which is attached to the terminal phenyl ring), and two big yellow contours in the R_1 and R_3 regions, which indicated that bulky groups in R_4 region were favored for Limk1 inhibition activity ($IC_{50Limk1}$ = 43 nM for **27** vs 142 nM for **18**), and bulky groups in R_3 and R_1 regions were disfavored for Limk1 inhibition activity ($IC_{50Limk1}$ = 1090 nM for **23**, 9240 nM for **24**, >10,000 nM for **25** vs 35 nM for **22**, and $IC_{50Limk1}$ = 710 nM for **17** vs 62 nM for **12**). According to Figure 3C and D, there was a big yellow contour at the 6-member ring side of the bottom pyrrolopyrimidine and the 2-position of middle phenyl ring, and some green contours at the terminal phenyl ring. These data suggested that bulky groups at the bottom pyrimidine side and bulky groups in the R_1 region were disfavored for Limk1/ROCK2 selectivity ($\Delta pIC_{50selectivity}$ = 0.999 for **17** vs 1.414 for **12**), and bulky groups in the R_2 region were favored for Limk1/ROCK2 selectivity ($\Delta pIC_{50selectivity}$ = 2.205 for **36** with 4-CH_3, 2.225 for **33** with 4-Cl, 2.225 for **32** with 3-Cl vs 2.184 for **27**, and $\Delta pIC_{50selectivity}$ = 1.414 for **12** with 3-$CONHCH(CH_3)_2$ vs 1.221 for **18**).

2.3.2. Contour maps of electrostatic field

The electrostatic field contour maps were shown in Figure 4. According to Figure 4A and B, there were both blue contours and red contours in the R_4 region, which suggested that groups with an appropriate charge would benefit the Limk1 inhibition. For example, CH_2CH_2OH and $CH_2CH_2NH_2$ were both good for Limk1 inhibitory activity ($pIC_{50Limk1}$ = 43 nM for **27** vs 142 nM for **18**, and 27 nM for **40** vs 35 nM for **22**). In Figure 4A, there was a red contour in the R_1 region which suggested that an electronegative group such as F was favored for Limk1 inhibition. For example, compound **16** had a lower IC_{50} than inhibitor **12** ($pIC_{50Limk1}$ = 18 - nM for **16** vs 62 nM for **12**). According to Figure 4C and D, there were a red contour around the 4-position of the terminal phenyl ring (R_2 region), which indicated that electronegative groups such as Cl were favored for selectivity, for example, the selectivity of **33** was better than **27** ($\Delta pIC_{50selectivity}$ = 2.241 for **33** vs 2.184 for **27**).

2.3.3. Contour maps of hydrophobic and H-bond donor/acceptor field

Contour maps of hydrophobic and H-bond donor/acceptor field were shown in Figure 5. As shown in Figure 5A and B, there were big white contours at the R_4 region and big yellow contours at the 4-position of the terminal phenyl ring, which demonstrated that hydrophilic group such as $-CH_2CH_2OH$ in the R_4 region and hydrophobic group such as CH_3 in the R_2 region were favored for both the Limk1 inhibitory activity and the Limk1/ROCK2 selectivity ($IC_{50Limk1}$ = 43 nM and $\Delta pIC_{50selectivity}$ = 2.184 for **27** vs 142 nM and 1.221 for **18**, and $IC_{50Limk1}$ = 37 nM and $\Delta pIC_{50selectivity}$ = 2.205 for **36** vs 43 nM and 2.184 for **27**).

Table 1
The structures and experimental IC_{50} values of urea-based Limk inhibitors

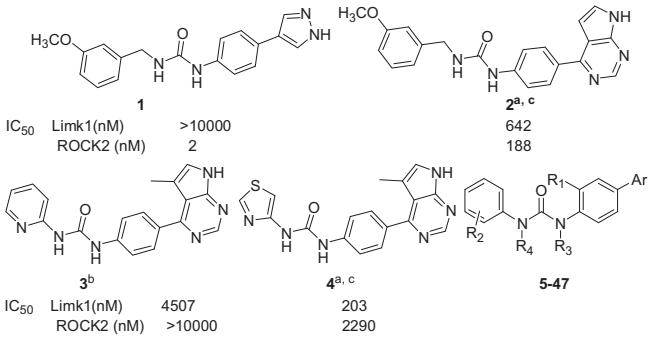

Compd	R_1	R_2	R_3	R_4	Ar	Limk1 IC_{50} (nM)	ROCK2 IC_{50} (nM)
5[a,c]	H	3-CONHCH$(CH_3)_2$	H	H		201	1365
6	H	3-CONHCH$(CH_3)_2$	H	H		>10,000	45
7	H	3-CONHCH$(CH_3)_2$	H	H		>10,000	90
8	H	3-CONHCH$(CH_3)_2$	H	H		>10,000	166
9	H	3-CONHCH$(CH_3)_2$	H	H		>10,000	132
10	H	3-CONHCH$(CH_3)_2$	H	H		>10,000	247
11[a,c]	H	3-CONHCH$(CH_3)_2$	H	H		1527	5570
12[a,c]	H	3-CONHCH$(CH_3)_2$	H	H		62	1608
13[b]	H	3-CONHCH$(CH_3)_2$	H	H		80	>10,000
14[a]	H	3-CONHCH$(CH_3)_2$	H	H		80	>10,000
15[a,c]	CF_3	3-CONHCH$(CH_3)_2$	H	H		60	976
16[a,c]	F	3-CONHCH$(CH_3)_2$	H	H		18	781
17[a,c]	$-OCH_2CH_2N(CH_3)_2$	3-CONHCH$(CH_3)_2$	H	H		710	7083
18[a,d]	H	H	H	H		142	2358
19[a,c]	H	3-F	H	H		315	5421
20[b,c]	H	2-OCH_3	H	H		283	6652
21[a,c]	H	3-OCH_3	H	H		75	2572

Table 1 (*continued*)

Compd	R_1	R_2	R_3	R_4	Ar	Limk1 IC_{50} (nM)	ROCK2 IC_{50} (nM)
22[a]	H	4-OCH_3	H	H		35	>10,000
23[a]	H	4-OCH_3	CH_3	H		1090	NR
24[a]	H	4-OCH_3		H		9240	NR
25	H	4-OCH_3		H		>10,000	NR
26[a]	H	H	H			368	NR
27[b,c]	H	H	H	CH_2CH_2OH		43	6565
28[b,d]	H	2-F	H	CH_2CH_2OH		132	1605
29[a,c]	H	3-F	H	CH_2CH_2OH		101	1898
30[b,c]	H	4-F	H	CH_2CH_2OH		86	3239
31[b,c]	H	2-Cl	H	CH_2CH_2OH		58	3339
32[b,d]	H	3-Cl	H	CH_2CH_2OH		67	11,270
33[a,d]	H	4-Cl	H	CH_2CH_2OH		25	4357
34[a]	H	2-CH_3	H	CH_2CH_2OH		350	>10,000
35[a,d]	H	3-CH_3	H	CH_2CH_2OH		151	8940
36[b,c]	H	4-CH_3	H	CH_2CH_2OH		37	5932
37[a]	H	2-OCH_3	H	CH_2CH_2OH		913	>10,000
38[a,c]	H	3-OCH_3	H	CH_2CH_2OH		100	3219
39[a]	H	4-OCH_3	H	CH_2CH_2OH		53	>10,000
40[a]	H	4-OCH_3	H	$CH_2CH_2NH_2$		27	NR
41[a]	H	4-Cl	H	$CH_2CH_2NH_2$		21	NR
42[a]	H	4-OCH_3	H	$CH_2CH_2N(CH_3)_2$		47	NR
43[a]	H	4-Cl	H	$CH_2CH_2N(CH_3)_2$		20	NR

(*continued on next page*)

Table 1 (*continued*)

Compd	R_1	R_2	R_3	R_4	Ar	Limk1 IC_{50} (nM)	ROCK2 IC_{50} (nM)
44[b]	F	4-Cl	H	CH_2CH_2OH		21	NR
45[a]	F	4-Cl	H	$CH_2CH_2NH_2$		21	NR
46[a]	F	4-Cl	H	$CH_2CH_2N(CH_3)_2$		19	NR
47[a]	F	4-Cl	H	$CH_2CH_2OCH_3$		8	NR

[a] Training set of 3D-QSAR models.
[b] Test set of 3D-QSAR models.
[c] Training set of 3D-QSSR models.
[d] Test set of 3D-QSSR models.

Table 2
Statistical parameters of 3D-QSAR and 3D-QSSR models

	3D-QSAR model		3D-QSSR model	
	CoMFA	CoMSIA	CoMFA	CoMSIA
q^2	0.618	0.572	0.561	0.541
NOC[a]	8	5	7	7
r^2	0.995	0.943	0.995	0.994
SEE	0.06	0.185	0.058	0.068
F-value	501.848	80.136	273.753	199.531
Contribution				
Steric	0.441	0.116	0.407	0.137
Electrostatic	0.559	0.369	0.593	0.167
H-acceptor	—	0.139	—	0.139
H-donor	—	0.186	—	0.104
Hydrophobic	—	0.191	—	0.453

[a] Optimal number of principal components.

In Figure 5C, the N atom of the urea linker attached to the terminal phenyl ring was surrounded by two big purple contours from both the upper and the down sides, which revealed that a unsubstituted NH was not as good as an alkylated N atom for the Limk1 inhibitory activity. For example, the $IC_{50Limk1}$ is 142 nM for compound **18** while that for inhibitor **27** is 43 nM. In Figure 5D, cyan contours occupied the R_4 region, which showed that groups containing H-bond donor moieties, such as CH_2CH_2OH and CH_2-CH_2NH_2, were favored for the Limk1/ROCK2 selectivity. For example, compound **27** exhibited a better inhibitory activity and a higher selectivity than compound **18** ($\Delta pIC_{50selectivity}$ = 2.205 for **27** vs 1.221 for **18**). In Figure 5E, there were magenta contours around the R_4 region, which demonstrated that groups with a H-bond acceptor, such as $-CH_2CH_2OCH_3$ and $-CH_2CH_2N(CH_3)_2$, were favored for Limk1 inhibition. For example, compounds **46** and **47** were among the most potent Limk inhibitors. In Figure 5F, the R_4 region was covered by a big red contour, which indicated that groups with a H-bond acceptor were disfavored and groups containing a H-bond donor were favored for the Limk1/ROCK2 selectivity ($\Delta pIC_{50selectivity}$ = 2.205 for **27** vs 1.221 for **18**).

2.4. Docking results

Docking protocols are widely used to explore the binding affinities of ligands. We further explored the difference of Limk1 inhibitory activity and Limk1/ROCK2 selectivity at the amino acid level through molecular docking in order to find more valuable information for designing potent and selective Limk inhibitors.

The structures of compounds **12** and **5** were similar with **12** having one more methyl group at the 3-position of bottom pyrrolopyrimidine ring. Inhibitor **12** exhibited a 3-fold higher Limk1 potency. However, it had a similar ROCK2 inhibition potency to compound **5** ($IC_{50Limk1}$ = 62 nM for **12** and 201 nM for **5**, $IC_{50ROCK2}$ = 1608 nM for **12** and 1365 nM for **5**). Docking **12** and **5** into the binding site of human Limk1 (PDB: 3S95) demonstrated that there were four H-bonds and one cation–π interaction in both **3S95-12** and **3S95-5** complexes (Fig. 6). However, there was an alkyl hydrophobic interaction between the $-CH_3$ group from the bottom pyrrolopyrimidine ring of inhibitor **12** and residues Leu467 and Ala353 of Limk1, which is likely the reason that inhibitor **12** had a higher Limk1 inhibitory activity than inhibitor **5**. So 3-methyl pyrrolopyrimidine moiety should be kept as a key structure unit in further deign of potent and selective Limk inhibitors.

Compound **33** had the highest selectivity ($\Delta pIC_{50selectivity}$ = 2.241) and compound **2** had the lowest selectivity ($\Delta pIC_{50selectivity}$ = −0.534). They were both docked into the ATP-binding pockets of human Limk1 (PDB: 3S95) and human ROCK2 (PDB: 4L6Q) (Fig. 7). In the **3S95-33** complex, there were three H-bonds between the pyrrolopyrimidine ring and residues Ile416, Glu414 and Thr413. A fourth H-bond was formed between the OH group and the carbonyl group of Lys347. In addition, a cation–π interaction was formed between the terminal phenyl ring and His464. Both H-bonds interactions and hydrophobic interactions contributed to the high Limk1 affinity of compound **33** (Fig. 7A). On the other hand, only H-bonds were formed between compound **2** and residues Ile416 and Glu414 in the **3S95-2** complex (Fig. 7B). Therefore, the higher Limk1 inhibition activity of compound **33** compared to **2** ($IC_{50Limk1}$ = 25 nM for **33** vs $IC_{50Limk1}$ = 642 nM for **2**) is likely due to the hydrophobic interactions from the terminal phenyl ring and the H-bond interaction at the R_4 region.

Previous studies demonstrated that both H-bonds and hydrophobic interactions contributed to the high activity of urea-based ROCK2 inhibitors and the residues for H-bonds were Glu170, Met172, Lys121 and Asp176.[43,44] As shown in Figure 7C, only one H-bond (between NH (N_1) and Met172) was formed in the **4L6Q-33** complex, which is likely the reason for the low ROCK2 inhibition of **33** ($IC_{50ROCK2}$ = 4357 nM). In the **4L6Q-2** complex, four H-bonds and one cation–π interaction were formed. The residues for H-bonds were Glu170, Met172 and Lys121, and the residue for cation–π interaction was Phe384. The distance between the

Table 3
Experimental and predicted values

Compd	Actual $pIC_{50Limk1}$[a]	3D-QSAR models					
		CoMFA			CoMSIA		
		Predicted $pIC_{50Limk1}$[a]	Residual $\Delta pIC_{50activity}$[b]	Residual rate[c] (%)	Predicted $pIC_{50Limk1}$[a]	Residual $\Delta pIC_{50activity}$[b]	Residual rate[c] (%)
Training set							
2	6.192	6.215	−0.023	−0.37	6.345	−0.153	−2.5
4	6.693	6.720	−0.027	−0.40	6.662	0.031	0.46
5	6.697	6.691	0.006	0.09	6.834	−0.137	−2.0
11	5.816	5.773	0.043	0.73	5.695	0.121	2.1
12	7.208	7.166	0.042	0.58	7.129	0.079	1.1
13	7.097	7.138	−0.041	−0.57	7.036	0.061	0.85
14	7.097	7.087	0.010	0.14	7.196	−0.099	−1.4
15	7.222	7.195	0.027	0.37	7.258	−0.036	−0.49
16	7.745	7.758	−0.013	−0.16	7.528	0.217	2.8
17	6.149	6.152	−0.003	−0.05	6.122	0.027	0.44
19	6.502	6.538	−0.036	−0.55	6.905	−0.403	−6.1
20	6.548	6.511	0.037	0.56	6.370	0.178	2.7
21	7.125	7.108	0.017	0.23	6.952	0.173	2.4
22	7.456	7.446	0.010	0.13	7.498	−0.042	−0.56
23	5.963	5.944	0.019	0.31	5.889	0.074	1.2
24	5.034	5.079	−0.045	−0.89	5.039	−0.005	−0.1
29	6.996	6.981	0.015	0.21	6.892	0.104	1.4
33	7.602	7.498	0.104	1.36	7.328	0.274	3.6
34	6.456	6.475	−0.019	−0.29	6.721	−0.265	−4.1
35	6.821	6.879	−0.058	−0.85	7.017	−0.196	−2.8
36	7.432	7.377	0.055	0.74	7.128	0.304	4.1
37	6.040	5.980	0.060	0.99	6.183	−0.143	−2.4
38	7.000	7.090	−0.090	−1.2	6.898	0.102	1.4
39	7.276	7.289	−0.013	−0.17	7.509	−0.233	−3.2
40	7.569	7.547	0.022	0.29	7.722	−0.153	−2.0
41	7.678	7.740	−0.038	−0.49	6.854	0.142	1.8
44	7.678	7.821	−0.143	−1.8	7.817	−0.139	−1.8
45	7.678	7.625	0.053	0.69	7.697	−0.019	−0.24
46	7.721	7.736	−0.015	−0.19	7.743	−0.022	−0.28
47	8.096	8.028	0.068	0.83	7.937	0.159	2.0
Test set							
3	5.346	5.831	−0.485	−9.0	5.878	−0.532	−9.9
18	6.848	6.195	0.653	9.5	6.017	0.831	12
26	6.434	6.720	−0.286	−4.4	6.811	−0.377	−5.8
27	7.367	7.231	0.136	1.8	6.976	0.391	5.3
28	6.879	7.104	−0.225	−3.2	6.506	0.373	5.4
30	7.066	7.723	−0.657	−9.2	7.328	−0.262	−3.7
31	7.237	6.628	0.609	8.4	6.736	0.501	6.9
32	7.173	7.417	−0.244	−3.4	7.133	0.040	0.55
42	7.328	7.686	−0.358	−4.8	7.339	−0.011	−0.15
43	7.699	7.358	0.341	4.4	7.151	0.548	7.1

Compd	Actual $\Delta pIC_{50selectivity}$[d]	3D-QSSR models					
		CoMFA			CoMSIA		
		Predicted $\Delta pIC_{50selectivity}$[d]	Residual $\Delta\Delta pIC_{50selectivity}$[e]	Residual rate[f] (%)	Predicted $\Delta pIC_{50selectivity}$[d]	Residual $\Delta\Delta pIC_{50selectivity}$[e]	Residual rate[f] (%)
Training set							
2	−0.534	−0.524	−0.01	1.8	−0.507	−0.027	5
4	1.053	1.053	0	0	1.034	0.019	1.8
5	0.832	0.832	0	0	0.807	0.025	3
11	0.562	0.549	0.013	2.3	0.572	−0.01	−1.7
12	1.414	1.403	0.011	0.77	1.415	−0.001	−0.07
15	1.211	1.226	−0.015	−1.2	1.208	0.003	0.24
16	1.638	1.646	−0.008	−0.48	1.67	−0.032	−1.9
17	0.999	0.999	0	0	0.995	0.004	0.4
19	1.236	1.164	0.072	0.48	1.104	0.132	10.6
20	1.371	1.363	0.008	0.58	1.404	−0.033	−2.4
21	1.535	1.592	−0.057	−3.7	1.542	−0.007	−0.45
27	2.184	2.078	0.106	4.8	2.075	0.109	4.9
29	1.274	1.33	−0.056	−4.3	1.303	−0.029	−2.2
30	1.576	1.61	−0.034	−2.1	1.637	−0.061	−3.8
31	1.761	1.735	0.026	1.5	1.802	−0.041	−2.3
36	2.205	2.272	−0.067	−3	2.239	−0.034	−1.5
38	1.508	1.496	0.012	0.79	1.525	−0.017	−1.1
Test set							
18	1.221	0.788	0.433	35	0.919	0.302	24
28	1.084	1.432	0.348	32	0.849	0.235	21

(*continued on next page*)

Table 3 (*continued*)

Compd	Actual $\Delta pIC_{50selectivity}$[d]	3D-QSSR models					
		CoMFA			CoMSIA		
		Predicted $\Delta pIC_{50selectivity}$[d]	Residual $\Delta\Delta pIC_{50selectivity}$[e]	Residual rate[f] (%)	Predicted $\Delta pIC_{50selectivity}$[d]	Residual $\Delta\Delta pIC_{50selectivity}$[e]	Residual rate[f] (%)
32	2.225	2.190	0.035	1.6	1.824	0.401	18
33	2.241	2.193	0.048	2.1	1.992	0.249	11
35	1.772	2.158	−0.386	−21	2.291	−0.519	−29

[a] $pIC_{50Limk1} = -\log IC_{50Limk1}$.
[b] Residual $\Delta pIC_{50activity}$ = actual $pIC_{50Limk1}$ − predicted $pIC_{50Limk1}$.
[c] Residual rate = $\Delta pIC_{50activity}$/actual $pIC_{50Limk1}$.
[d] $\Delta pIC_{50selectivity} = pIC_{50Limk1} - pIC_{50ROCK2}$.
[e] Residual $\Delta\Delta pIC_{50selectivity}$ = actual $\Delta pIC_{50selectivity}$ − predicted $\Delta pIC_{50selectivity}$.
[f] Residual rate = $\Delta\Delta pIC_{50selectivity}$/actual $\Delta pIC_{50selectivity}$.

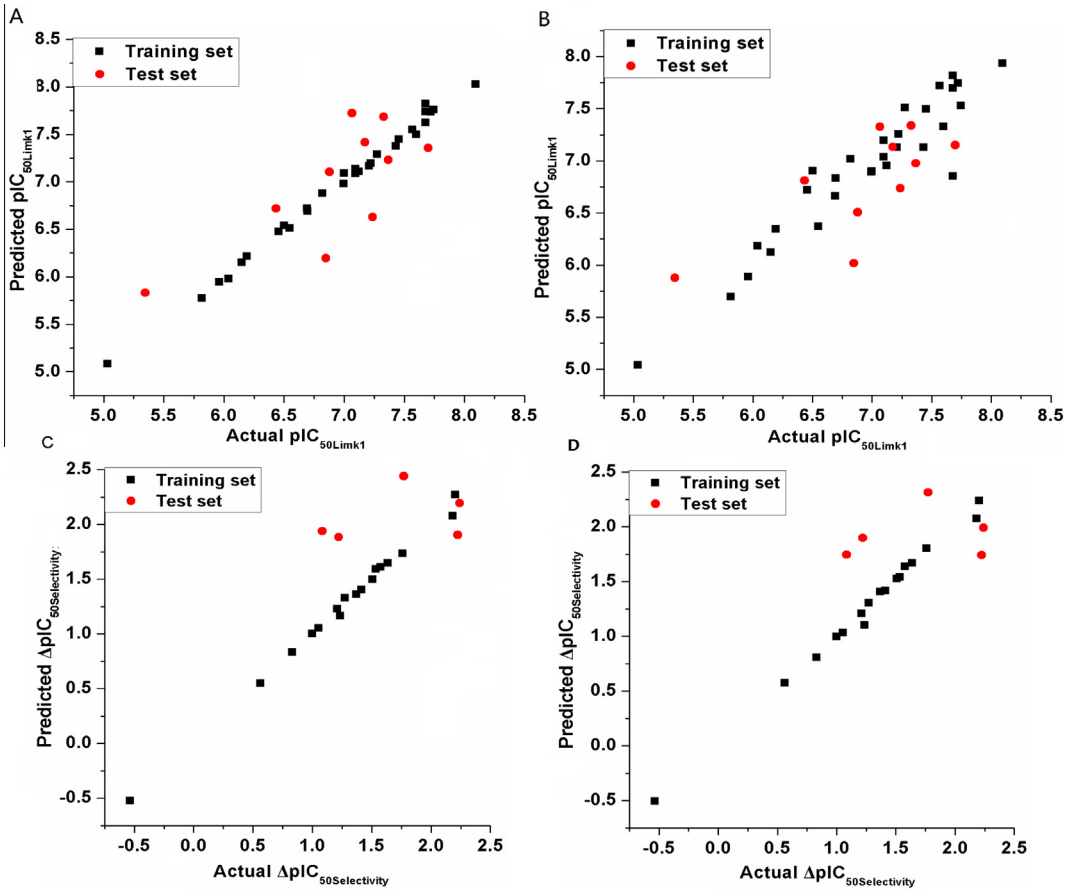

Figure 1. Plots of actual versus predicted values. (A) CoMFA 3D-QSAR model. (B) CoMSIA 3D-QSAR model. (C) CoMFA 3D-QSSR model. (D) CoMSIA 3D-QSSR model.

urea carbonyl group and the terminal phenyl ring of **33** was shorter than that of **2** (two and three backbone atoms for **33** and **2**, respectively), and the structural elements of compounds **33** could not fit well into the hydrophobic pocket. Therefore, compound **33** exhibited lower ROCK2 potency than **2** ($IC_{50ROCK2}$ = 4357 nM for **33** vs $IC_{50ROCK2}$ = 188 nM for **2**). So carbonyl group-aromatic ring system (CONH-Ar) will be good structure moiety in next inhibitors' design.

2.5. MD simulations results

In order to validate the docking accuracy, we performed 5 ns MD simulation for **3S95-33** complex (Fig. 8). The total-energy reduced sharply at the beginning, and basically remained at 4249 ± 150 KJ/mol from 3.5 ns to 5.0 ns, which showed that the final structure of the 5.0 ns MDs was stable. Both initial and final docked inhibitors were in the same binding pocket and their pharmacophore structures were basically consistent, which demonstrated that docking results were reliable.

2.6. Designs of urea-based Limk1 inhibitors

Optimal computational results should have the following advantages: the results fit the rule well and it can provide guidance for inhibitor designs. Therefore, we test our computational results through synthesis and biological evaluation of newly designed Limk1 inhibitors. Molecular docking showed that 3-methyl

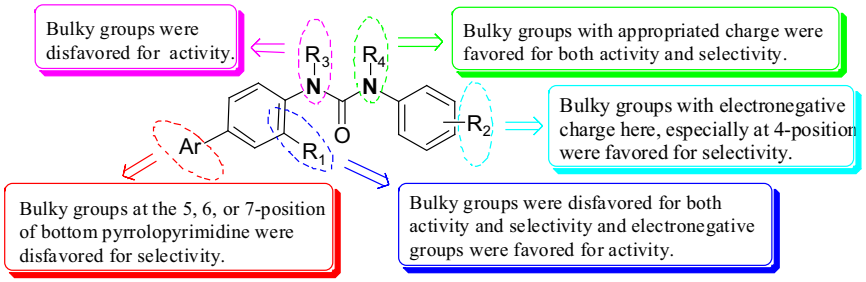

Figure 2. Structure–activity/selectivity relationships derived from 3D-QSAR and 3D-QSSR studies.

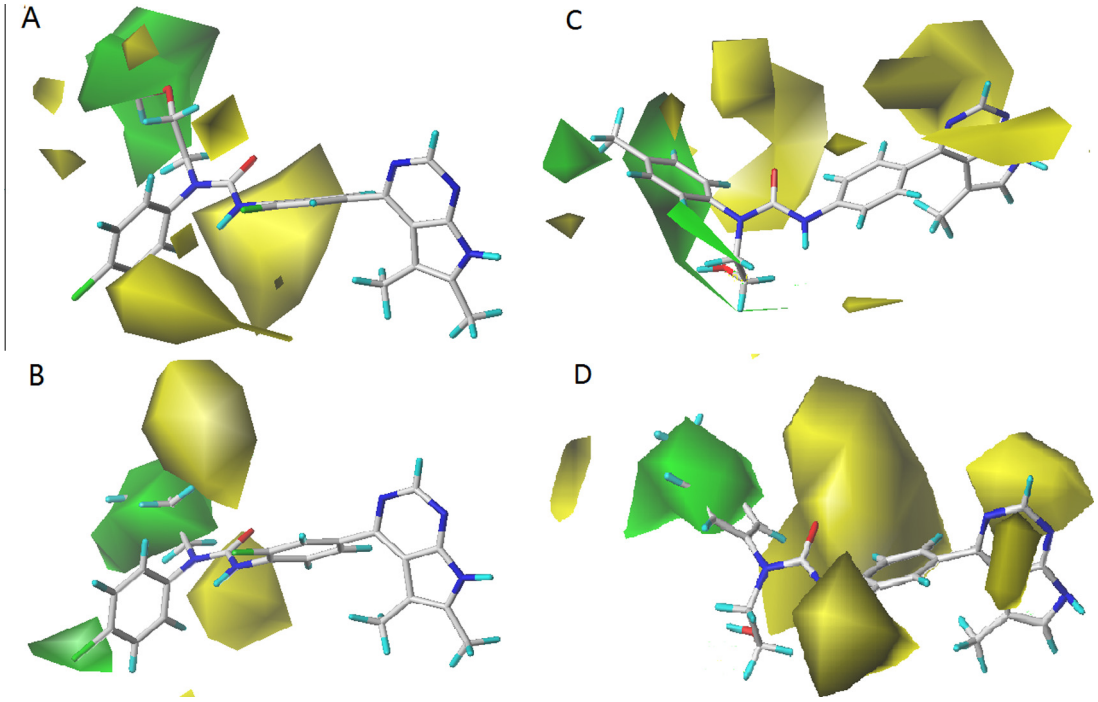

Figure 3. Counter maps of steric field. (A) CoMFA 3D-QSAR model. (B) CoMSIA 3D-QSAR model. (C) CoMFA 3D-QSSR model. (D) CoMSIA 3D-QSSR model. Bulky groups were favored in the green regions and disfavored in the yellow regions.

pyrrolopyrimidine moiety (Fig. 6) and carbonyl-aromatic ring system (CONH-Ar, Fig. 7) were good structure units and should be kept in further design of potent and selective Limk inhibitors. Contour map of electrostatic field suggested that electronegative group such as F, or $-CH_2CH_2OH$ with appropriate charges in the R_4 region was favored for Limk1 inhibition (Fig. 4). So fragments including 3-methyl pyrrolopyrimidine at the bottom aromatic region, carbonyl group-aromatic ring system (CONH-Ar), F atom in the R_1 region, and $-CH_2CH_2OH$ in the R_4 region were introduced in the newly designs of Limk inhibitors, which were favored for both Limk1 inhibition and the Limk1/ROCK2 selectivity. Compounds (**D1**–**D5**) were therefore designed and synthesized, and the synthetic route and biochemical data of them were shown in Figure 9 and Table 4, respectively. Remarkably, the IC_{50} values obtained from computational models and biochemical assays were quite similar and within the allowed error range (less than 10 times) except the IC_{50} value of **D1** against ROCK2 which was out of the test window.[45] **D1** exhibited a better Limk1 inhibitory activity compared to **22** ($IC_{50Limk1}$ = 10 nM for **D1** vs 35 nM for **22**). **D5** also exhibited a better Limk1 potency and an enhanced Limk1/ROCK2 selectivity compared to inhibitor **18** ($IC_{50Limk1}$ = 85 nM for **D2** vs 142 nM for **18**, and 53-fold Limk1/ROCK2 selectivity for **D2** vs 16-fold for **18**). Changing the tailor phenyl ring to pyridine or pyrimidine also led to potent and selective Limk inhibitors ($IC_{50Limk1}$ = 11 nM for **D2**, 19 nM for **D3**, and 55 nM for **D4**, and $IC_{50ROCK2}$ = 2114 nM for **D2**, 2011 nM for **D3**, and 1021 nM for **D4**). So the computational results obtained in this work were effective for designing new Limk1 inhibitors.

3. Conclusion

From the data set collected from bis-aryl urea derivatives as Limk inhibitors, CoMFA 3D-QSAR models, CoMSIA 3D-QSAR models, CoMFA 3D-QSSR models, and CoMSIA 3D-QSSR models were built up, and the structure–activity/selectivity relationships were obtained by analyzing the contour maps of CoMFA and CoMSIA models. Molecular docking further demonstrated that hydrophobic interaction with residues Leu467 and Ala353 was one of the key elements for Limk1 inhibition. A 5 ns MD simulations certified the reliability of docking results. Finally, new compounds were designed, synthesized, and biologically evaluated, and these compounds exhibited good Limk inhibitory activity and selectivity. These results demonstrated that the computational results were effective for designing highly potent and Limk1/ROCK2 selective

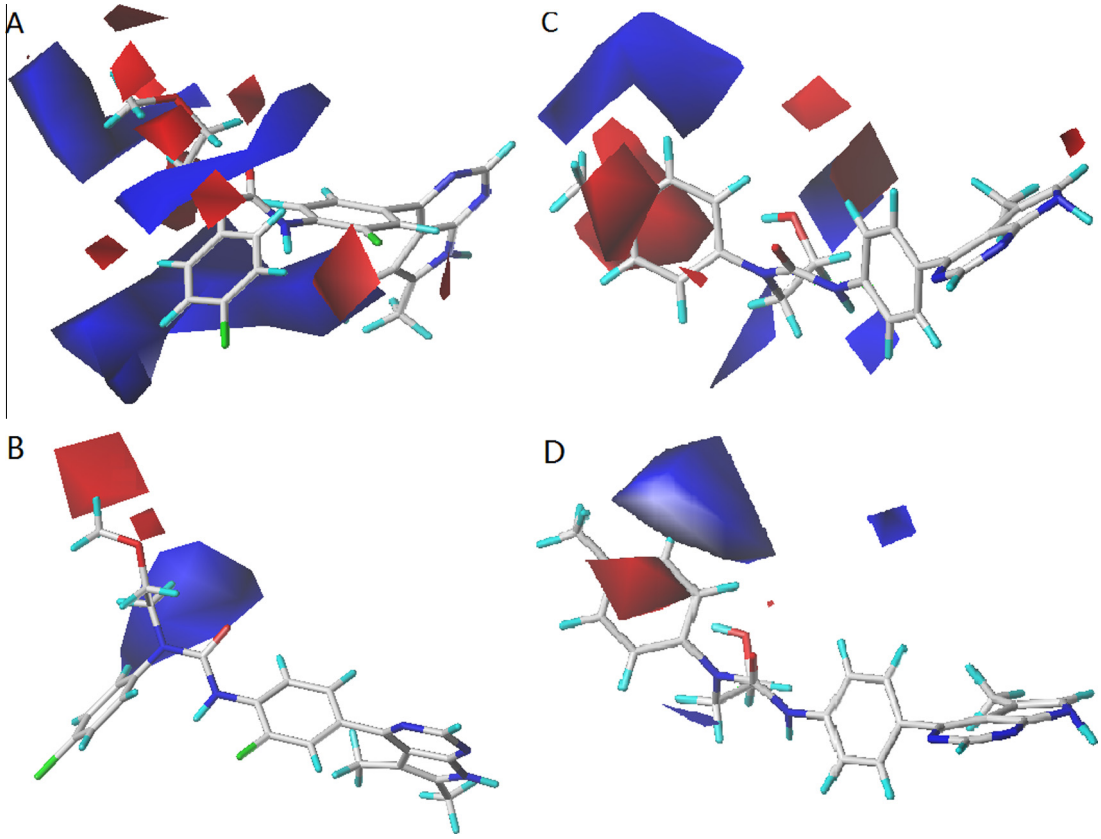

Figure 4. Contour maps of electrostatic field. (A) CoMFA 3D-QSAR model. (B) CoMSIA 3D-QSAR model. (C) CoMFA 3D-QSSR model. (D) CoMSIA 3D-QSSR model. Electropositive groups were favored in the blue regions, and electronegative groups were favored in the red regions.

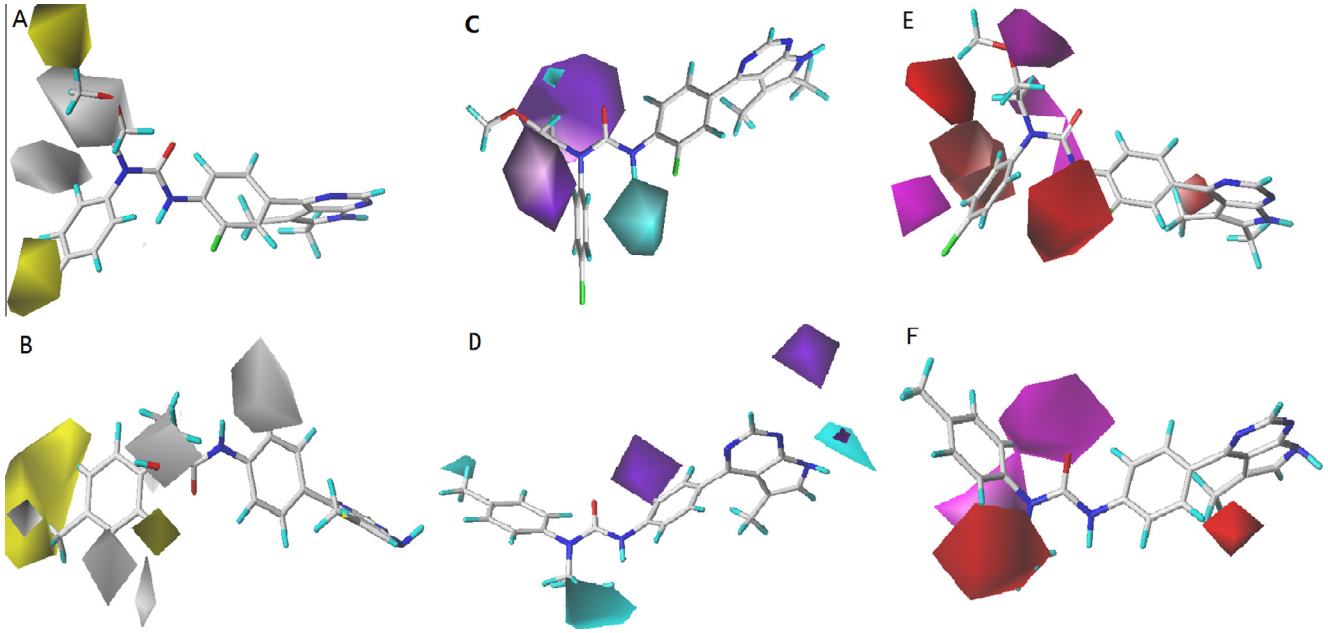

Figure 5. Contour maps of hydrophobic and H-bond donor/acceptor field. (A) Hydrophobic field of CoMSIA 3D-QSAR model. (B) Hydrophobic field of CoMSIA 3D-QSSR model. (C) H-bond donor fields of CoMSIA 3D-QSAR model. (D) H-bond donor fields of CoMSIA 3D-QSSR model. (E) H-bond acceptor fields of CoMSIA 3D-QSAR model. (F) H-bond acceptor fields of CoMSIA 3D-QSSR model. Hydrophobic groups were favored in the yellow regions and disfavored in the white regions. H-bond donor groups were favored the cyan regions and disfavored in the purple regions. H-bond acceptor groups were favored in the magenta regions and disfavored in red regions.

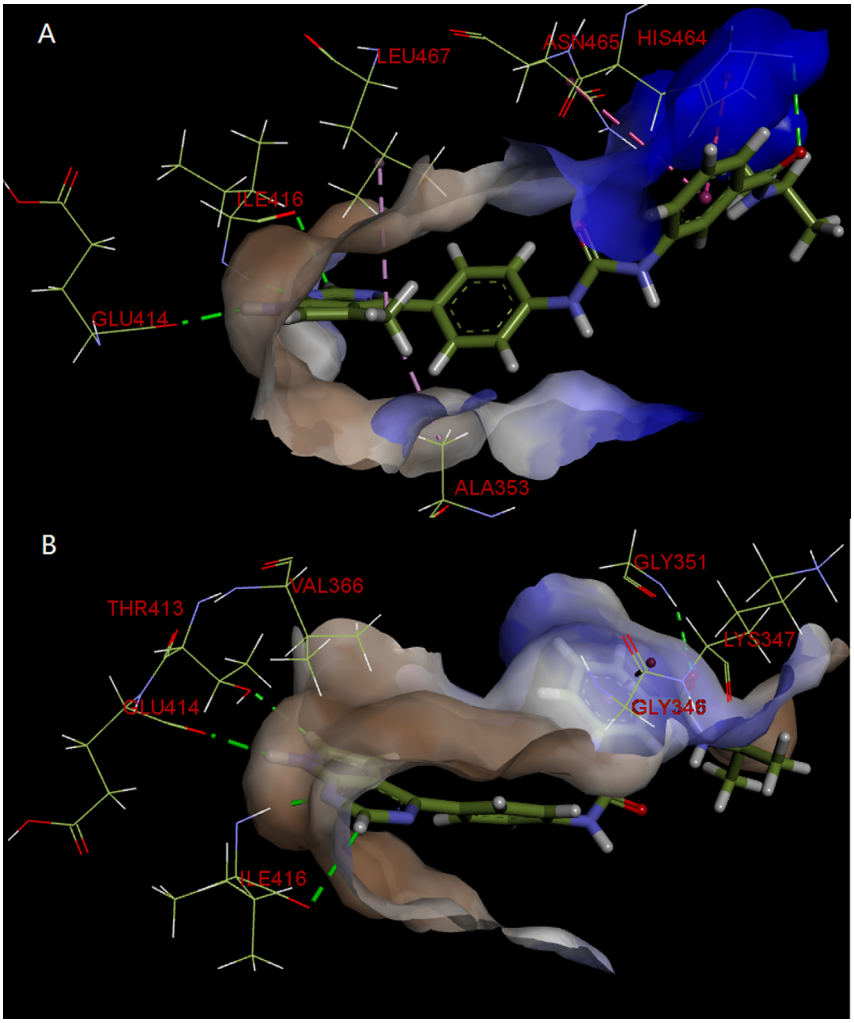

Figure 6. Docking results. (A) Docking of **12** into the binding site of Limk1. (B) Docking of **5** into the binding site of Limk1. Hydrogen bonds were shown as green lines, alkyl hydrophobic interactions were shown as pink lines, and cation–π interactions were shown as red lines.

Limk inhibitors. The exploration of the F-substitution effects on the Limk inhibitory activity and selectivity using computational tools is underway in our labs and will be published in due course.

4. Experimental

Commercially available reagents and anhydrous solvents were used without further purification unless otherwise specified. Thin layer chromatography (TLC) analyses were performed with precoated silica gel 60 F254. The mass spectra were recorded by LC/MS with Finnigan LCQ Advantage MAX spectrometer of Thermo Electron®. Flash chromatography was performed on prepacked columns of silica gel (230–400 Mesh, 40–63 μm) by CombiFlash® with EtOAc/hexane or MeOH/DCM as eluent. The preparative HPLC was performed on SunFire C18 OBD 10 μm (30 × 250 mm) with CH_3CN + 50% MeOH/H_2O + 0.1% TFA as eluent to purify the targeted compounds. Analytic HPLC was performed on Agilent technologies 1200 series with CH_3CN (Solvent B)/H_2O + 0.9% CH_3CN + 0.1% TFA (Solvent A) as eluent and the targeted products were detected by UV in the detection range of 215–310 nm. All compounds were determined to be >95% pure by this method. NMR spectra were recorded with a Bruker® 400 MHz spectrometer at ambient temperature with the residual solvent peaks as internal standards. The line positions of multiplets were given in ppm (δ) and the coupling constants (J) were given in Hertz. The high-resolution mass spectra (HRMS, electrospray ionization) experiments were performed with Thermo Finnigan Orbitrap mass analyzer. Data were acquired in the positive ion mode at resolving power of 100,000 at m/z 400. Calibration was performed with an external calibration mixture immediately prior to analysis.

4.1. Synthetic procedure and structural characterization of D1–D5

4-Methoxy-phenylamine, 6-methyl-pyridin-3-ylamine, 2-methyl-pyridin-4-ylamine, pyrimidin-5-ylamine, or 2-phenylamino-ethanol (0.2 mmol) was added to the solution of 4-bromo-2-fluoro-1-isocyanato-benzene (0.2 mmol) in DCM (1 mL). The mixture was stirred at room temperature for 2 h. Then, the solvent was removed in vacuo to give the crude bromide **A** for next step without further purification. Bis-(pinacolato)diboron (0.24 mmol), **A** (0.2 mmol), and $PdCl_2$(dppf) (0.02 mmol) were dissolved in degassed dioxane (5 mL). After refluxing for 2 h, the mixture was diluted with water and extracted with ethyl acetate (3 × 5 mL). The organic layers were combined, dried over anhydrous Na_2SO_4 and concentrated in vacuo to give crude boronic acid pinacol ester **B**. Finally, **B** (0.3 mmol) and 4-chloro-5-methyl-7*H*-pyrrolo[2,3-*d*]pyrimidine (0.2 mmol) were dissolved in degassed 5:1 dioxane/H_2O. $Pd(PPh_3)_4$ (0.02 mmol) and 2 M solution of K_2CO_3 (0.6 mmol) were added sequentially under argon and the mixture was heated at 95 °C for 2 h. After cooling to room temperature, the mixture was diluted with water and extracted with ethyl

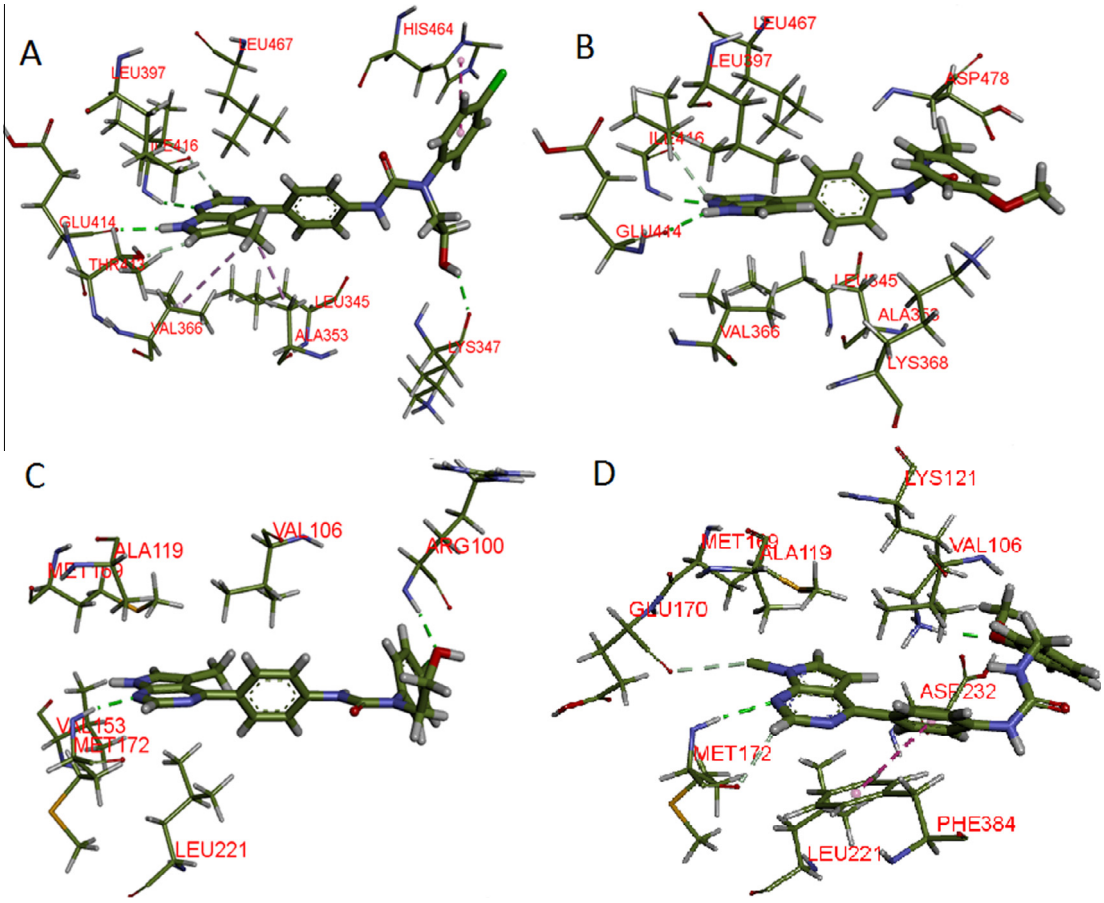

Figure 7. Docking results. (A) Docking of compound **33** into the binding site of Limk1. (B) Docking of compound **2** into the binding site of Limk1. (C) Docking of compound **33** into the binding site of ROCK2. (D) Docking of compound **2** into the binding site of ROCK2. Hydrogen bonds were shown as green lines, alkyl hydrophobic interactions were shown as pink lines, and cation–π interactions were shown as red lines.

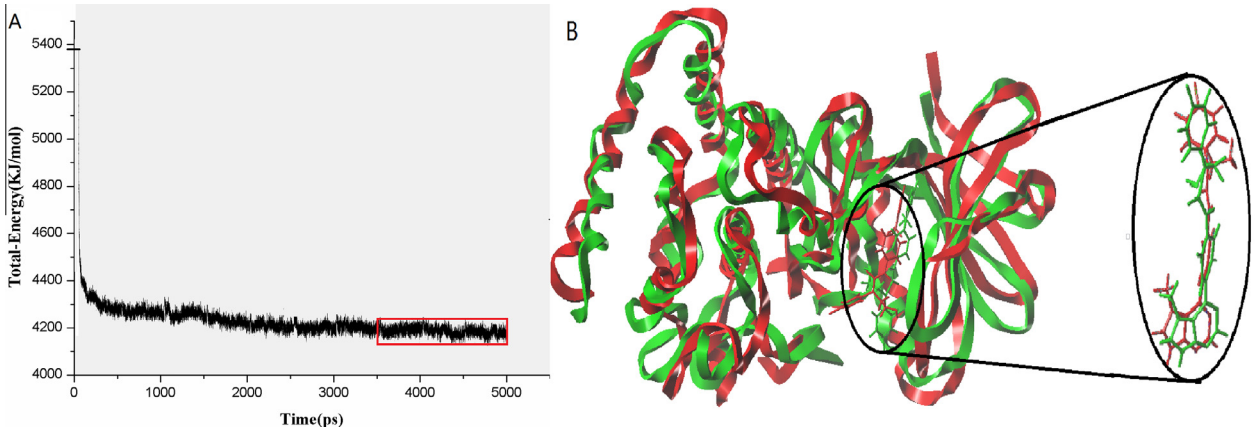

Figure 8. MDs results. (A) Plot of total energy versus time. (B) **3S95-33** complex. The initial structure represent in magenta and the final structure represent in green.

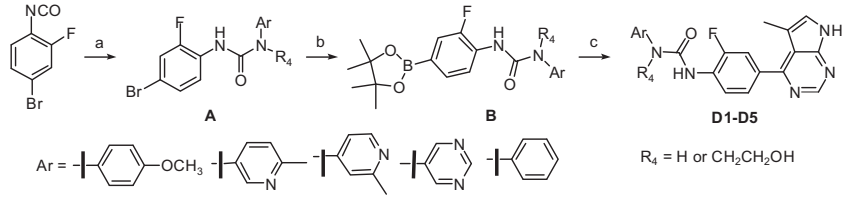

Figure 9. Synthesis of newly designed Limk inhibitors. Reagents and conditions: (a) Ar-NHR$_4$, DCM, 0 °C; (b) bis(pinacolato)diboron, PdCl$_2$dppf, dioxane, reflux; (c) 4-chloro-5-methyl-7*H*-pyrrolo[2,3-*d*]pyrimidine, Pd(PPh$_3$)$_4$, dioxane/H$_2$O, 95 °C.

Table 4
Biochemical data of **D1**–**D5**

Compd	Experimental IC_{50} (nM)		Pred. IC_{50} (nM) by CoMFA		Pred. IC_{50} (nM) by CoMSIA	
	Limk1	ROCK2	Limk1	ROCK2	Limk1	ROCK2
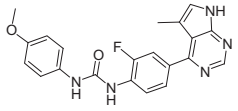 **D1**	10	>20,000	65	2187	98	1840
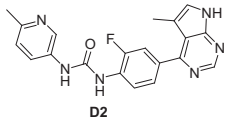 **D2**	11	2114	17	2152	45	5572
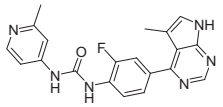 **D3**	19	2011	53	933	82	3793
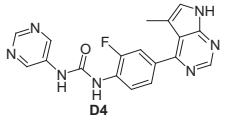 **D4**	55	1021	57	276	479	893
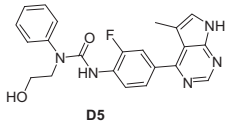 **D5**	85	4508	111	3140	181	2333

acetate (3 × 5 mL). The organic layers were combined, dried over anhydrous Na_2SO_4 and concentrated in vacuo. The residue was then purified by preparative HPLC to give the targeted product **D1**–**D5** as white solids.

4.1.1. 1-[2-Fluoro-4-(5-methyl-7*H*-pyrrolo[2,3-*d*]pyrimidin-4-yl)-phenyl]-3-(4-methoxy-phenyl)-urea (D1)

50% yield in 3 steps. Purity >99.9% (detected by UV at 215 nm, 230 nm, 254 nm, 280 nm, and 310 nm). ^{1}H NMR (DMSO-d_6, 400 MHz) δ 12.01 (s, br, 1H), 8.99 (s, 1H), 8.75 (s, 1H), 8.69–8.68 (m, 1H), 8.39–8.37 (m, 1H), 7.60–7.56 (m, 1H), 7.54–7.50 (m, 1H), 7.49–7.46 (m, 1H), 7.40–7.38 (m, 3H), 6.91–6.89 (m, 2H), 3.73 (s, 3H), 2.09 (s, 3H); ^{13}C NMR (DMSO-d_6, 100 MHz) δ 154.70, 152.39, 152.15, 149.78, 148.14, 132.25, 129.73, 129.63, 128.95, 127.00, 126.48, 119.95, 119.20, 116.14, 115.93, 114.81, 114.05, 109.98, 55.14, 12.73; LC/MS (M+H$^+$): 392.10; HRMS (ESI-Orbitrap) Calcd for $C_{21}H_{18}FN_5O_2$: 392.1523 [M+H$^+$], Found 392.1546.

4.1.2. 1-[2-Fluoro-4-(5-methyl-7*H*-pyrrolo[2,3-*d*]pyrimidin-4-yl)-phenyl]-3-(6-methyl-pyridin-3-yl)-urea; compound with methane (D2)

48% yield in 3 steps. Purity >99.9% (detected by UV at 215 nm, 230 nm, 254 nm, 280 nm, and 310 nm). ^{1}H NMR (DMSO-d_6, 400 MHz) δ 12.20 (s, br, 1H), 9.41 (s, 1H), 8.90–8.80 (m, 2H), 8.41–8.40 (m, 1H), 8.23–8.21 (m, 1H), 7.89 (s, 1H), 7.71–7.65 (m, 2H), 7.48–7.5 (m, 1H), 2.34 (s, 3H), 2.07 (s, 3H); ^{13}C NMR (DMSO-d_6, 100 MHz) δ 158.11, 154.38, 153.97, 152.09, 145.87, 142.96, 142.34, 138.77, 130.42, 129.16, 128.37, 128.20, 127.32, 125.31, 124.73, 118.69, 114.50, 111.55, 20.95, 12.53; LC/MS (M+H$^+$): 377.13; HRMS (ESI-Orbitrap) Calcd for $C_{20}H_{18}FN_6O$: 377.1526 [M+H$^+$], Found 377.1515.

4.1.3. 1-[2-Fluoro-4-(5-methyl-7*H*-pyrrolo[2,3-*d*]pyrimidin-4-yl)-phenyl]-3-(2-methyl-pyridin-4-yl)-urea (D3)

47% yield in 3 steps. Purity >99.9% (detected by UV at 215 nm, 230 nm, 254 nm, 280 nm, and 310 nm). ^{1}H NMR (DMSO-d_6, 400 MHz) δ 12.19 (s, br, 1H), 9.71 (s, 1H), 8.83 (s, 1H), 8.29–8.19 (m, 3H), 8.01–8.00 (m, 2H), 7.70–7.68 (m, 1H), 7.48–7.46 (m, 1H), 7.39–7.37 (m, 1H), 2.34 (s, 3H), 2.09 (s, 3H); ^{13}C NMR (DMSO-d_6, 100 MHz) δ 158.40, 158.06, 154.37, 153.84, 152.08, 145.75, 143.02, 140.61, 136.21, 131.13, 130.43, 129.30, 128.47, 127.64, 127.09, 118.82, 114.50, 111.62, 17.31, 12.51; LC/MS (M+H$^+$): 377.14; HRMS (ESI-Orbitrap) Calcd for $C_{20}H_{18}FN_6O$: 377.1526 [M+H$^+$], Found 377.1509.

4.1.4. 1-[2-Fluoro-4-(5-methyl-7*H*-pyrrolo[2,3-*d*]pyrimidin-4-yl)-phenyl]-3-pyrimidin-5-yl-urea (D4)

51% yield in 3 steps. Purity >99.9% (detected by UV at 215 nm, 230 nm, 254 nm, 280 nm, and 310 nm). ^{1}H NMR (DMSO-d_6, 400 MHz) δ 12.56 (s, br, 1H), 9.18 (s, 1H), 8.94–8.19 (m, 2H), 7.78–7.48 (m, 6H), 7.32–7.28 (m, 2H), 7.01–6.98 (m, 1H), 2.10 (s, 3H); ^{13}C NMR (DMSO-d_6, 100 MHz) δ 154.43, 152.14, 146.62, 142.62, 142.54, 130.30, 129.37, 129.09, 127.78, 127.66, 127.59, 126.52, 119.18, 118.67, 114.56, 111.08, 12.61; LC/MS (M+H$^+$): 364.17; HRMS (ESI-Orbitrap) Calcd for $C_{18}H_{15}FN_7O$: 364.1322 [M+H$^+$], Found 364.1341.

4.1.5. 3-[2-Fluoro-4-(5-methyl-7*H*-pyrrolo[2,3-*d*]pyrimidin-4-yl)-phenyl]-1-(2-hydroxy-ethyl)-1-phenyl-urea (D5)

45% yield in 3 steps. Purity >99.9% (detected by UV at 215 nm, 230 nm, 254 nm, 280 nm, and 310 nm). ^{1}H NMR (DMSO-d_6, 400 MHz) δ 12.59 (s, br, 1H), 8.89 (s, 1H), 8.75 (s, 1H), 7.66–7.50 (m, 6H), 7.42–7.26 (m, 3H), 3.72 (t, J = 6.4 Hz, 2H), 3.57 (d, J = 6.4 Hz, 2H), 2.07 (s, 3H); ^{13}C NMR (DMSO-d_6, 100 MHz) δ 159.17, 128.37, 128.03, 156.71, 154.39, 153.62, 152.07, 145.55, 143.00, 130.39, 129.81, 128.90, 125.09, 119.00, 116.45, 114.51, 111.76, 59.33, 51.98, 12.47; LC/MS (M+H$^+$): 416.17; HRMS (ESI-Orbitrap) Calcd for $C_{22}H_{21}FN_5O_2$: 416.1679 [M+H$^+$], Found 416.1692.

4.2. Limk1 assay

Limk1 biochemical assay was carried out in Reaction Biology Corporation and followed the protocols described on its Web site. Newly designed compounds (**D1**–**D5**) and control compound

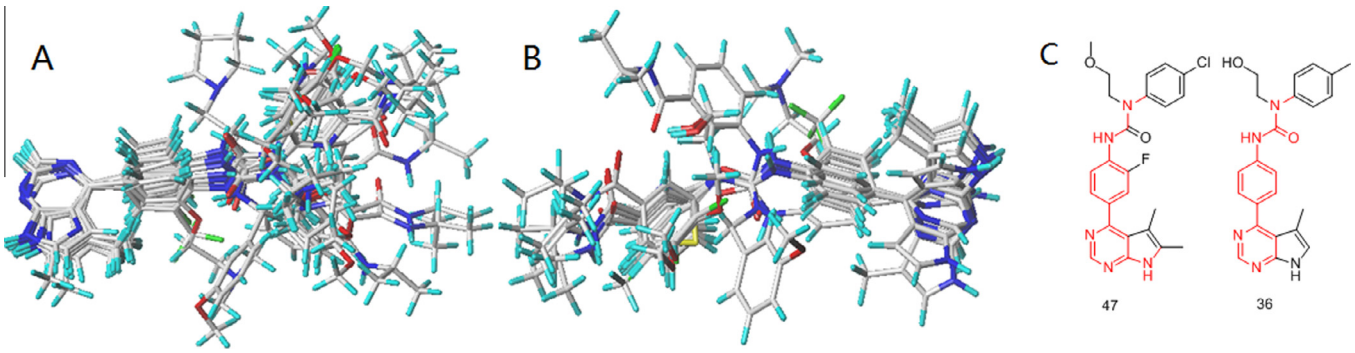

Figure 10. The alignments of training set molecules. (A) The alignment of 3D-QSAR models with **47** as the template compound. (B) The alignment of 3D-QSSR models with **36** as the template compound. (C) Common substructures were marked in red.

staurosporine were tested in 10-dose IC_{50} mode with 3-fold series dilution starting at 10 μM with IC_{50} measurements. Reactions were carried out at 10 μM ATP, 1 μM substrate cofilin, and 50 nM Limk1 (final concentration).

4.3. ROCK2 assay

Assays were performed using the STK2 kinase system from Cisbio. A 5 μL mixture of a 1 μM STK2 substrate and ATP (ROCK-II: 20 μM) in STK-buffer was added to the wells of the 384-well plate using a BioRAPTR FRD Workstation (Aurora Discovery, Carlsbad, CA). Twenty nanoliters of test compound was then dispensed using a 384-head offline Pintool system (GNF Systems, San Diego, CA). The reaction was started by adding either 5 μL of 0.5 nM ROCK-II in STK-buffer. After 4 h at rt the reaction was stopped by adding 10 μL of 1× antibody and 62.5 nM Sa-XL in Detection Buffer. After 1 h incubation at rt, the plates were read on the Viewlux in HTRF mode.

4.4. Ligand preparation

The ligand preparation was performed using SYBYL 2.0. Energy minimization of all the compounds was processed using Tripos molecular mechanics force field with energy gradient criterion of 0.005 k cal/(Å mol), and the charges of Tripos force field were calculated by the Gasteiger method. Then the training set compounds were aligned on the template molecules by the alignment command in SYBYL. The optimal alignment for 3D-QSAR models and 3D-QSSR models were shown in Figure 10 and the common substructures were marked in red.

4.5. CoMFA and CoMSIA models

The optimal chemical conformations after ligand preparation were aligned and used directly to build CoMFA and CoMSIA models. 3D contour maps of steric and electrostatic fields in CoMFA models and five fields including steric, electrostatic, hydrophobic, hydrogen bond donor, and hydrogen bond acceptor in CoMSIA models were graphed using the Sybyl 2.0 program (Tripos, Inc., USA). The regression analysis was carried out using the PLS method and the final models were selected according to the statistical parameters.

4.6. Molecular docking

The crystal structures of human Limk1 and human ROCK2 for molecular docking were downloaded from RCSB Protein Data Bank (http:/www.rcsb.org/pdb/home/home.do, PDB: 3S95 for Limk1 and 4L6Q for ROCK2). All water molecules were removed and hydrogen atoms were added. Then, the end residues were repaired and protein was performed energy minimization. In the docking process, the protein was fixed while the ligands were flexible, the ligands were docked into the ATP-binding site of Limk1 or ROCK2 by a patented module in Surflex-Dock and the docked complex was evaluated by empirical scoring function. By default, 30 conformations were generated for each ligand and their scores were forecasted based on the strength of receptor–ligand interactions. The docked conformation with best score was selected for further studies.

4.7. MD simulations

The MD simulations were carried out in Sybyl 2.0 software. The conformation with best score was picked as initial conformation. Constant temperature (300 K) and volume were maintained with the time constant for a heat bath coupling of 100 fs. The time step of 1 fs was used to integrate the equations of motion, and the snapshot time was 100 fs and MD target was limited in the range of 3 Å with ligand as the core. The Boltzmann initial velocity was used to start the simulation. Other parameters were set by default in Sybyl 2.0.

Acknowledgments

The work was supported by National Natural Science Foundation of China (Grant No. 21502117). Support from Prof. Gang Zhao and Prof. Guanjun Wang was also greatly appreciated.

References and notes

1. Manetti, F. *Drug Discovery Today* **2012**, *17*, 81.
2. Scott, R. W.; Olson, M. F. *J. Mol. Med.* **2007**, *85*, 555.
3. Goodwin, N. C.; Cianchetta, G.; Burgoon, H. A.; Healy, J.; Mabon, R.; Strobel, E. D.; Allen, J.; Wang, S. L.; Hamman, B. D.; Rawlins, D. B. *ACS Med. Chem. Lett.* **2015**, *6*, 53.
4. Manetti, F. *Med. Res. Rev.* **2012**, *32*, 968.
5. Nadella, K. S.; Saji, M.; Jacob, N. K.; Pavel, E.; Ringel, M. D.; Kirschner, L. S. *EMBO Rep.* **2009**, *10*, 599.
6. Goyal, P.; Pandey, D.; Siess, W. *J. Biol. Chem.* **2006**, *281*, 25223.
7. Arber, S.; Barbayannis, F. A.; Hanser, H.; Schneider, C.; Stanyon, C. A.; Bernard, O.; Caroni, P. *Nature* **1998**, *393*, 805.
8. Misra, U. K.; Deedwania, R.; Pizzo, S. V. *J. Biol. Chem.* **2005**, *280*, 26278.
9. Efrat, M. F.; Roni, R.; Galit, E. S.; Roni, H.; Shmuel, C.; Yoel, K.; Wolfson, H. J. *Oncotarget* **2012**, *3*, 629.
10. Jiang, X. S.; Wassif, C. A.; Backlund, P. S.; Song, L.; Holtzclaw, L. A.; Li, Z.; Yergey, A. L.; Porter, F. D. *Hum. Mol. Gen.* **2010**, *19*, 1347.
11. Sun, L.; Guo, C. N.; Wang, T.; Li, X.; Li, G. J.; Luo, Y. L.; Xiao, S. F. *J. Alzheimers Dis.* **2014**, *42*, 543.
12. Saal, K. Ann.; Koch, J. C.; Tatenhorst, L.; Szego, E. M.; Ribas, V. T.; Michel, U.; Baehr, M.; Toenges, L.; Lingor, P. *Neurobiol. Dis.* **2015**, *73*, 150.
13. Matsumoto, N.; Kitani, R.; Kalinec, F. *Commun. Integr. Biol.* **2011**, *4*, 208.
14. Honma, M.; Benitah, S. A.; Watt, F. M. *Mol. Biol. Cell.* **2006**, *17*, 1888.
15. Zhou, Y.; Yuge, A.; Rajah, A. M.; Unek, G.; Rinaudo, P. F.; Maltepe, E. *Am. J. Pathol.* **2014**, *184*, 3321.

16. Low, S. K.; Zembutsu, H.; Takahashi, A.; Kamatani, N.; Cha, P. C.; Hosono, N.; Kubo, M.; Matsuda, K.; Nakamura, Y. *J. Hum. Genet.* **2011**, *56*, 211.
17. Harrison, B. A.; Whitlock, N. A.; Voronkov, M. V.; Almstead, Z. Y.; Gu, K. J.; Mabon, R.; Gardyan, M.; Hamman, B. D.; Allen, J.; Gopinathan, S.; McKnight, B.; Crist, M.; Zhang, Y.; Liu, Y.; Courtney, L. F.; Key, B.; Zhou, J.; Patel, N.; Yates, P. W.; Liu, Q.; Wilson, A. G.; Kimball, S. D.; Crosson, C. E.; Rice, D. S.; Rawlins, D. B. *J. Med. Chem.* **2009**, *52*, 6515.
18. Xu, X. H.; Guo, J.; Vorster, P.; Wu, Y. *Commun. Integr. Biol.* **2012**, *5*, 381.
19. Vorster, P. J.; Guo, J.; Yoder, A.; Wang, W.; Zheng, Y.; Xu, X.; Yu, D.; Spear, M.; Wu, Y. *J. Biol. Chem.* **2011**, *286*, 12554.
20. Wen, X.; Ding, L.; Wang, J. J.; Qi, M.; Hammonds, J.; Chu, H.; Chen, X.; Hunter, E.; Spearman, P. *J. Virol.* **2014**, *88*, 6906.
21. Chen, P. X.; Zeng, M. J.; Zhao, Y.; Fang, X. L. *Oncol. Rep.* **2014**, *32*, 2070.
22. Xu, M.; Chen, G.; Wang, S.; Liao, M.; Frank, J. A.; Bower, K. A.; Zhang, Z.; Shi, X.; Luo, J. *PLoS One* **2012**, *7*, e47721.
23. Xia, H.; Sun, S. J.; Wang, B.; Wang, T.; Liang, C. Y.; Li, G.; Huang, C. B.; Qi, D. L.; Chu, X. Y. *Int. J. Mol. Sci.* **2014**, *15*, 11973.
24. Moretti, R. M.; Mai, S.; Marelli, M. M.; Rizzi, F.; Bettuzzi, S.; Limonta, P. *Int. J. Oncol.* **2011**, *39*, 225.
25. Scott, R. W.; Hooper, S.; Crighton, D.; Li, A.; Konig, I.; Munro, J.; Trivier, E.; Wickman, G.; Morin, P.; Croft, D. R.; Dawson, J.; Machesky, L.; Anderson, K. I.; Sahai, E. A.; Olson, M. F. *J. Cell Biol.* **2010**, *191*, 169.
26. Morin, P.; Wickman, G.; Munro, J.; Inman, G. J.; Olson, M. F. *Eur. J. Cell Biol.* **2011**, *90*, 13.
27. Vlecken, D. H.; Bagowski, C. P. *Zebrafish* **2009**, *6*, 433.
28. Sleebs, B. E.; Levit, A.; Street, I. P.; Falk, H.; Hammonds, T.; Wong, A. C.; Charles, M. D.; Olson, M. F.; Baell, J. B. *Med. Chem. Commun.* **2011**, *2*, 977.
29. Sleebs, B. E.; Ganame, D.; Levit, A.; Street, I. P.; Gregg, A.; Falk, H.; Baell, J. B. *Med. Chem. Commun.* **2011**, *2*, 982.
30. Sleebs, B. E.; Nikolakopoulos, G.; Street, I. P.; Falk, H.; Baell, J. B. *Bioorg. Med. Chem. Lett.* **2011**, *21*, 5992.
31. Boland, S.; Bourin, A.; Alen, J.; Geraets, J.; Schroeders, P.; Castermans, K.; Kindt, N.; Boumans, N.; Panitti, L.; Vanormelingen, J.; Fransen, S.; Velde, S. V.; Defert, O. *Bioorg. Med. Chem. Lett.* **2015**, *25*, 4005.
32. Ross-Macdonald, P.; de Silva, H.; Guo, Q.; Xiao, H.; Hung, C. Y.; Penhallow, B.; Markwalder, J.; He, L. Q.; Attar, R. M.; Lin, T. A.; Seitz, S.; Tilford, C.; Wardwell-Swanson, J.; Jackson, D. *Mol. Cancer Ther.* **2008**, *7*, 3490.
33. Mashiach-Farkash, E.; Rak, R.; Elad-Sfadia, G.; Haklai, R.; Carmeli, S.; Kloog, Y.; Wolfson, H. J. *Oncotarget* **2012**, *3*, 629.
34. He, L. Q.; Seitz, S. P.; Trainor, G. L.; Tortolani, D.; Vaccaro, W.; Poss, M.; Tarby, C. M.; Tokarski, J. S.; Penhallow, B.; Hung, C. Y.; Attar, R.; Lin, T. A. *Bioorg. Med. Chem. Lett.* **2012**, *22*, 5995.
35. Harrison, B. A.; Whitlock, N. A.; Voronkov, M. V.; Almstead, Z. Y.; Gu, K. J.; Mabon, R.; Gardyan, M.; Hamman, B. D.; Allen, J.; Gopinathan, S.; McKnight, B.; Crist, M.; Zhang, Y. L.; Liu, Y.; Courtney, L. F.; Key, B.; Zhou, J. L.; Patel, N.; Yates, P. W.; Liu, Q. Y.; Wilson, A. G. F.; Kimball, S. D.; Crosson, C. E.; Rice, D. S.; Rawlins, D. B. *J. Med. Chem.* **2009**, *52*, 6515.
36. Harrison, B. A.; Almstead, Z. Y.; Burgoon, H.; Gardyan, M.; Goodwin, N. C.; Healy, J.; Liu, Y.; Mabon, R.; Marinelli, B.; Samala, L.; Zhang, Y. L.; Stouch, T. R.; Whitlock, N. A.; Gopinathan, S.; McKnight, B.; Wang, S. L.; Patel, N.; Wilson, A. G. E.; Hamman, B. D.; Rice, D. S.; Rawlins, D. B. *ACS Med. Chem. Lett.* **2015**, *6*, 84.
37. Sun, J. R.; Lan, P.; Sun, P. H.; Chen, W. M. *Lett. Drug Des. Discovery* **2011**, *8*, 229.
38. Shen, M. Y.; Zhou, S. Y.; Li, Y. Y.; Li, D.; Hou, T. J. *Mol. BioSyst.* **2013**, *9*, 2435.
39. Mezna, M.; Wong, A. C.; Ainger, M.; Scott, R. W.; Hammonds, T.; Olson, M. F. *J. Biomol. Screening* **2012**, *17*, 460.
40. Yin, Y.; Zheng, K.; Eid, N.; Howard, S.; Jeong, J.; Yi, F.; Guo, J.; Park, C.; Bibian, M.; Wu, W.; Hernandez, P.; Wu, Y.; Luo, J. L.; LoGrasso, P. V.; Feng, Y. *J. Med. Chem.* **2015**, *58*, 1846.
41. Ding, M.; Yin, Y.; Wu, F. H.; Cui, J. X.; Zhou, H.; Sun, G. F.; Jiang, Y. *Bioorg. Med. Chem.* **2015**, *23*, 2505.
42. Sun, N. Y.; Lu, T.; Chen, Y. D.; Hao, L. H.; Xu, Y.; Li, R. J. *Acta Phys. Chim. Sin.* **2009**, *25*, 645.
43. Yin, Y.; Cameron, M. D.; Lin, L.; Khan, S.; Schroer, T.; Grant, W.; Pocas, J.; Chen, Y. T.; Schurer, S.; Pachori, A.; LoGrasso, P.; Feng, Y. B. *ACS Med. Chem. Lett.* **2010**, *1*, 175.
44. Yin, Y.; Lin, L.; Ruiz, C.; Khan, S.; Cameron, M. D.; Grant, W.; Pocas, J.; Eid, N.; Park, H.; Schroter, T.; LoGrasso, P.; Feng, Y. B. *J. Med. Chem.* **2013**, *56*, 3568.
45. Patel, P. D.; Patel, M. R.; Kaushik-Basu, N.; Talele, T. T. *J. Chem. Inf. Model.* **2008**, *48*, 42.